World Scientific
www.worldscientific.com

DYNAMIC PERFORMANCE OF POST-BUCKLED PRECOMPRESSED PIEZOELECTRIC ACTUATOR ELEMENTS

GEORGIOS GIANNOPOULOS[*]

European Commission, Joint Research Center
Chemical Assessment and Testing Unit
Via E. Fermi 2749, 21027 (VA) Italy

MARK GROEN and ROELOF VOS

Faculty of Aerospace Engineering
Delft University of Technology
Delft, The Netherlands

RON BARRETT

Department of Aerospace Engineering
The University of Kansas, Lawrence, KS, USA

Post-buckled precompressed (PBP) piezoelectric elements have recently been used to enable a new class of actuators that are able to provide far higher deflections compared to the traditional bimorph piezoelectric actuators while maintaining full force and moment generating capabilities. Past research has proven that PBP actuators are capable of generating deflections three times higher than conventional bimorph actuators. In this paper, this work has been extended to the dynamic response realm and the performance of PBP actuators is investigated under various axial loads, at various actuation frequencies. Both analytical and finite element models have been developed in order to evaluate the performance of the actuator regarding the natural frequency shift under increased axial loads. Experimental verification has shown that the overall damping ratio of the structure is a function of the axial forces. Values derived from experiments have been used in the Finite Element model to predict the displacement output, phase angle shifting and end rotation. Numerical and analytical results correlate very well with the experiments and thus give credit to the formulation presented in this work.

Keywords: Post-buckled precompressed; piezoelectric; dynamic performance.

[*]Current Employement, work mainly performed during previous employment at Royal Military Academy Brussels.

Nomenclature

A = Normalized amplitude, −
B = Distributed coupling stiffness, N
b = Actuator width, m
c = Distributed damping coefficient, Ns/m^2
D = Distributed bending stiffness, Nm
d = Spring displacement, m
d_{31} = Piezoelectric charge constant, V/m
E = Stiffness, or electric field, N/m^2, V/m
F = Force, N
f = Forcing frequency, Hz
G = Shear stress, N/m^2
GF = Gauge Factor, −
t = Structure thickness, m
I = Moment of inertia, m^4
K = Stiffness, N/m
k = Spring stiffness, N/m
L = Length of beam, m
M = Mass or moment, kg, Nm
m = Distributed mass, kg/m^2
R = Resistance, Ω
r = Radius of curvature, m
t = Time, s
u = Displacement, m
V = Voltage, V
v = Vertical displacement, m
W = Work, Nm
x = Spacial coordinate, m
z = Spacial coordinate, m

Greek Symbols

α = Loss coefficient, N/m
δ = Differential, −
ϵ = Strain, m/m
ζ = Damping ratio, −
θ = End rotation, deg
ν = Poisson ratio, −
ρ = Density, kg/m^3
ϕ = Curvature, 1/m
ψ = Shape function, −
ω = Forcing frequency, rad/s

Subscripts and superscripts

$* =$ Equivalent
$a =$ Axial
$act =$ Actuator
$amp =$ Amplitude
$b =$ Bond
$dc =$ DC offset
$l =$ Laminate
$n =$ Natural
$p =$ Piezoelectric
$s =$ Substrate
$SE =$ Strain energy
$0 =$ Initial condition

Abbreviations

$DAQ =$ Data Acquisition Device
$FE =$ Finite Element
$PBP =$ Post-Buckled Precompressed
$SDOF =$ Single degree of freedom

1. Introduction

Piezoelectric actuators suffer from inherent incapability to deliver high mechanical deflection output combined with high moment generation. High deflection can be achieved at the expense of moment generation and vice versa. There exists a linear relationship that, until recently has defined the operational envelope of such structures. For actuation applications with high deflection output necessity amplification mechanisms were conceived tailored towards the application in miniature UAVs. The work of Barrett *et al.*[1−4] has shown how actuators can be embedded in small control surfaces, such that they are capable of providing a meaningful moment/displacement combination adequate for flight control. In Fig. 1, the moment/displacement trade off is clearly depicted providing thus a clear indication of the limitations of conventionally configured, linear adaptive actuators.

The problems that aeromechanicians have to face in order to use conventional, linear piezoelectric actuators for flight control are clearly depicted in Fig. 1. In general, the amount of moment that can be obtained at the maximum displacement is limited and thus the actuator cannot cope with overdesign loads. Although a raft of actuator amplification mechanisms are available for conventional piezoelectric actuators, all they generally do is trade force for deflection. Accordingly, the work per unit mass and volume simply goes down as these techniques are employed.
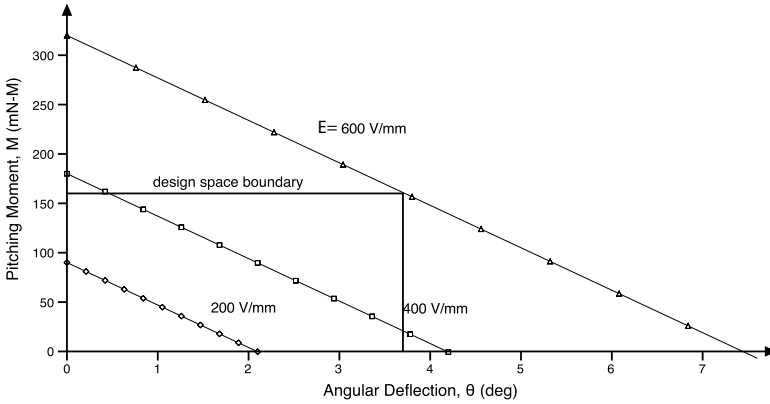
Fig. 1. Typical pitching moment versus deflection design space relationship for conventional, linear Microflex piezoelectric actuators driving a 5 cm semispan, 2 cm chord stabilator.[5]

Additionally, it is obvious that half of the available mechanical energy of the actuator goes essentially unused. Thus there is large room for improving the efficiency of these actuators.

Towards this direction the work of Lesieutre[6] was instrumental in demonstrating clearly that an actuator can have higher coupling coefficient (or transfer efficiency) than its active material. In order to achieve this target, a new class of mechanics was introduced, called post-buckled precompressed (PBP) actuators. Bender piezoelectric elements could exhibit much higher displacement generation with no moment reduction through the application of an additional axial force. This axial force essentially amplified any curvature that was originally introduced by the piezoelectric elements thereby magnifying the peak-to-peak deflection. This opened a new area of structural mechanics that although unintentional, could be used for flight control of airborne structures. At axial forces close to the perfect-column buckling load, snap-through buckling could occur which was investigated by Giannopoulos *et al.*[7,8] Piezoelectric bender actuators were examined experimentally and analytically in order to predict this highly non-linear behavior. Although snap-through mechanics were introduced to further increase the actuation capabilities of piezoelectric structures with axial forces, the highly nonlinear behavior of these structures rendered them inconvenient for integration into structures that were driven by controller circuits. Maurini *et al.* demonstrated numerically that using a two-parameter actuation approach makes it is possible to get quasi-static transitions between the two specular equilibria of the buckled beam, without any instability phenomenon (like snap-through buckling behavior).[9] This required the simultaneous actuation of the axial force and the actuation voltage. For many control mechanisms, however, a quasi static displacement is required for a constant axial force without the occurrence of instabilities.

In the domain of flight control based on PBP actuators the work that exists in literature is limited. In this context the work of Vos *et al.*,[10,11] De Breuker *et al.*[12]

and Barrett *et al.*[13,14] has been instrumental. They clearly demonstrated that non-linear mechanics can be applied successfully in airborne structures despite their inherent difficulty of combining the nonlinear mechanics with electronics and controllers. As is shown in the aforementioned works, PBP elements have been used for the flight control of UAVs, munitions and missiles.

Even though the simultaneous increase in moment and displacement output through the application of axial forces has worked well in quasi-static performance, it comes at the cost of reduced natural frequency. Obviously, the application of PBP elements for flight control imposes certain requirements on their dynamic behavior. The decrease of the natural frequencies and the corresponding increase in the overall damping ratio have been clearly depicted in the work of Groen *et al.*[15] Clearly the reduction in natural frequencies and damping increase have to be quantified in order to tailor such elements in case dynamic performance is of interest. Apart from the previously mentioned work of Groen *et al.* the authors have not been able to find any other similar contribution in the literature.

The present work aims to present a complete analysis of the dynamic performance of PBP elements. An analytical as well as a finite element (FE) model have been developed in order to accurately grasp the mechanics of these structures. The validity of these models has been backed-up by experimental results. It has been clearly demonstrated that indeed the precompression exerted on the PBP actuators alters significantly their behavior in the dynamic domain. It has been revealed that both the damping ratio as well as the natural frequencies of the actuator shift with increased compressive force.

2. Analytic Modeling using Virtual Work

Figure 2 shows a sketch of an example axially compressed beam in simply supported configuration. In this configuration the element is subjected to the end fixity conditions of: $\psi(0) = \psi(L) = 0$, where L is the length of the beam element and ψ is a shape function. The dimensions of this element are presented in Table 1, while the properties of the materials that constitute it are shown in Table 2.

The bimorph piezoelectric actuator element can be dynamically modeled as an oscillating Euler beam with an infinite amount of degrees of freedom. By imposing a
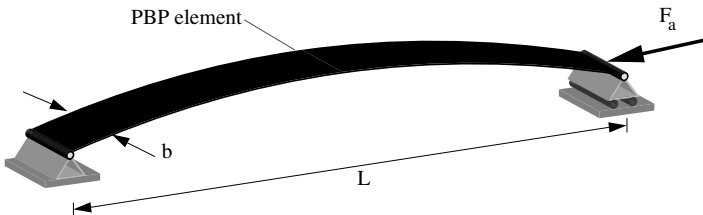

Fig. 2. Schematic representation of axially compressed PBP actuator element in simply supported configuration.

Table 1. Dimensions and stiffness coefficients of PBP element.

t_p μm	t_s μm	t_b μm	L mm	b mm	B_{act} kN	D_l Nm	$E_{3\,max}$ V/mm
267	76	102	230	11.2	10.5	3.82	660

Table 2. Material properties of evaluated PBP element.

	Piezoelectric	Substrate	Bond Line
Material	PZT 5A	Aluminum 1100-H18	Hysol 9412
Density, ρ (kg/m³)	7,800	2,700	2,400
Stiffness, E, (GPa)	61	70	1
Poisson's ratio, ν (−)	0.31	0.3	0.3

mode shape these infinite degrees of freedom are connected and the problem can be reduced to a single degree of freedom (SDOF) system of the form[16]:

$$M^*\ddot{v} + C^*\dot{v} + K^*v = F^*(t). \tag{2.1}$$

A shape function $\psi(x)$ multiplied by an amplitude $z(t)$ is used to prescribe the shape of the beam during the oscillation. In the present work a sinusoidal shape function has been used with $\psi(x) = \sin x$ and $0 < x < \pi$. Accordingly, $v(x,t) = \psi(x)z(t)$. By using the principle of virtual work[16] a virtual displacement, $\delta z(t)$ is imposed on the beam structure resulting in an amount of work, δW, done on the structure. Assuming an infinitesimal amount of virtual displacement $(\delta z(t) \to 0)$ yields the following:

$$\delta W = \Sigma F \cdot \delta z(t) = 0. \tag{2.2}$$

The virtual work done by the distributed mass, m, is represented by:

$$\delta W_I = -\left[m \int_0^L \psi^2(x)dx\right]\ddot{z}(t)\delta z(t), \tag{2.3}$$

Where the distributed mass is expressed as:

$$m = (2\rho_p t_p + 2\rho_b t_b + \rho_s t_s)b. \tag{2.4}$$

The work that is performed by the damping force is expressed by the following equation:

$$\delta W_{DE} = -c\left[\int_0^L \psi^2(x)dx\right]\dot{z}(t)\delta z(t). \tag{2.5}$$

The internal work is done by a moment, M, acting through a virtual curvature, $\delta\phi(x) : M = EIv''(x,t)\delta v''(x,t)$, or in terms of laminate stiffness, $M = D_l bv''(x,t)\delta v''(x,t)$, where D_l is the distributed bending stiffness of the laminate. Using

classical laminated plate theory (CLPT) this coefficients can be expanded as follows[18]:

$$D_l = E_s \frac{1}{1 - \nu_s^2} \frac{t_s^3}{12} + E_p \frac{1}{1 - \nu_p^2} \left[t_p \frac{(t_s + 2t_b)^2}{2} + (t_s + 2t_b)t_p^2 + \frac{2}{3}t_p^3 \right]. \qquad (2.6)$$

Substitution of the shape function and integration over the entire beam yields the virtual strain energy:

$$\delta W_{SE} = -\left[\int_0^L D_l b(\psi''(x))^2 dx \right] z(t)\delta z(t). \qquad (2.7)$$

Work done by the normal force, F_a, can be expressed as:

$$\delta W_N = \left[\int_0^L F_a(\psi'(x))^2 dx \right] z(t)\delta z(t). \qquad (2.8)$$

The actuation of the bimorph PZT element can be modeled by a distributed moment, $M(t) = B_{\text{act}} d_{31} E_3(t)b$, where B_{act} is the distributed coupling stiffness of the actuator elements, d_{31} is a piezoelectric charge content, and E_3 is the electric field strength. For the bimorph actuator element considered here, this coefficient can be calculated using the method laid out in Jones[18]:

$$B_{\text{act}} = E_p \frac{1 + \nu_p}{1 - \nu_p^2} (t_s t_p + 2t_b t_p + t_p^2). \qquad (2.9)$$

Analogous to the internal work, this distributed moment induces a rotation, $\delta\phi(x)$, which leads to:

$$\delta W_{\text{act}} = B_{\text{act}} d_{31} E_3(t)b \left[\int_0^L \psi''(x) dx \right] \delta z(t). \qquad (2.10)$$

By adding Eq. (2.3) through Eq. (2.10) the total virtual work can be found:

$$\delta W = \delta W_I + \delta W_{DE} + \delta W_{SE} + \delta W_N + \delta W_{\text{act}}. \qquad (2.11)$$

Substituting the expressions for each of the terms in Eq. (2.11) and letting $\delta z(t) \to 0$, results in the equation of motion for this system:

$$\left[m \int_0^L \psi^2(x) dx \right] \ddot{z} + \left[\int_0^L c\psi^2(x) dx \right] \dot{z} + \left[\int_0^L D_l b(\psi''(x))^2 - F_a(\psi'(x))^2 dx \right] z$$

$$= B_{\text{act}} d_{31} E_3(t)b \left[\int_0^L \psi''(x) dx \right]. \qquad (2.12)$$

Equation (2.12) is of the form of Eq. (2.1).

When a harmonic forcing function with a forcing frequency of ω is chosen for the electric field strength (i.e. $E_3(t) = E_3 \sin(\omega t)$), the following normalized response can be found:

$$A = \frac{1}{\sqrt{\left[1 - \left(\frac{\omega}{\omega_n} \right)^2 \right]^2 + \left[2\zeta\left(\frac{\omega}{\omega_n} \right) \right]^2}}. \qquad (2.13)$$

The natural frequency of the structure is calculated by the following equation:

$$\omega_n = \sqrt{\frac{K}{M}} = \sqrt{\frac{\int_0^L (D_l b(\psi''(x))^2 - F_a(\psi'(x))^2)dx}{m \int_0^L \psi^2(x)dx}}. \tag{2.14}$$

In the analytical model, structural damping is considered. Energy is dissipated internally within the material proportional to the square of the amplitude of vibration.[16,17] The damping ratio can be obtained from the following equation:

$$\zeta = \frac{\alpha}{2\pi k} \frac{\omega_n}{\omega}, \tag{2.15}$$

where α is the loss coefficient (constant). The use of the loss coefficient has been decided due to the fact that the damping ratio of the structure (as it will be shown later from the experimental results) is not constant.

3. Finite Element Analysis

3.1. *Model setup and assumptions*

In addition to the analytical model a finite element analysis has also been developed. The aim of this model is to investigate the response of piezoelectric structures in terms of displacements and frequency shifting due to the compressive loading and to compare with analytical models and experimental results. The added value of a finite element model is that it can grasp more phenomena such as various boundary conditions combined with nontrivial (or even optimal) geometries. In addition, the two operating modes for the piezoelectric layers (open and closed circuit) can be evaluated. In open circuit conditions the piezoelectric layer is allowed to develop a voltage between its two faces and thus store the electric energy that is developed due to its elastic deformation. In that case one face of the piezoelectric layer is considered to be grounded (zero voltage) while the other is free. Thus a voltage difference between the two faces can be developed as a result of the inherent capability of the piezoelectric layer to transform part of the elastic energy to electric energy. In fact it operates as a capacitor. In open circuit conditions both faces of the piezoelectric layer are grounded (zero voltage). Thus no voltage difference between the two faces can be developed and obviously no electric energy can be stored in the piezoelectric layer. In that case the capability of the piezoelectric layer to transform part of the elastic energy to electric energy is canceled and the piezoelectric layer performs as a normal structural material. It will be shown that proper analytical set-up of the model can yield very accurate results.

The model has been developed in ANSYS (Academic License). The finite element model is built using various types of eight-node finite elements. Although a model consisting of plate elements would seem more adequate for such analysis, in fact it is not applicable. The main reason for using brick elements is that due to the existence of piezoelectric material, the interfaces between the various material layers is

required for the application of the boundary electrical conditions. This choice can be potentially dangerous for the analysis due to the large aspect ratio of the structures ($L/t_{\text{act}} > 100$) that can lead to numerical instabilities which manifest themselves in erroneous results. In Fig. 4, the meshed geometry of the finite element model is shown.

The representation of the different materials of the piezoelectric structure requires various multiphysics models that are not included in all solid elements. Two types of eight-node solid elements had to be used. The SOLID5 (ANSYS nomenclature) is a piezoelectric finite element that supports nonlinear analysis, while SOLID45 is more adapted to conventional structural materials without multiphysics modeling requirements. The FE model parameters are shown in Table 3. The aluminum layer is divided into two layers through the thickness in order to facilitate the application of the boundary conditions in the middle layer of the structure. These are $u_x(0, y, t_{\text{act}}/2) = u_y(0, y, t_{\text{act}}/2) = u_z(0, y, t_{\text{act}}/2) = 0$, $u_y(L, y, t_{\text{act}}/2) = u_z(L, y, t_{\text{act}}/2) = 0$. The beam is free to displace at x-direction at the end of the beam ($u_x(L, y, t_{\text{act}}/2) \neq 0$).

The material properties introduced are the ones of the PZT 5A material. However, there are two important modifications that have taken place in order to adapt to the real structural properties. The structure that is evaluated in this work has an active length of 218 mm (230 mm with the end supports) with the end supports made of different material (Hysol 9412 epoxy with style #120 fiberglass cloth at 254 μm thickness epoxy). For the sake of accuracy this has been included in the FE model. The second modification is related to the flexural rigidity of the structure. Due to the fact that the length of the actuator significantly exceeds the maximum length of the available PZT 5A plates (72×72 mm) three pieces of the piezoelectric material had to be positioned next to each other on the aluminum substrate. As a consequence of the resulting seams the structure had reduced overall flexural rigidity. In order to appreciate the effect of this discontinuity of the piezoelectric elements, a three-point bend test took place in order to quantify the amount of the reduction of the flexural rigidity. The test revealed that the mean flexural rigidity (EI) has been reduced from the theoretical value of 0.0296 Nm^2 to 0.022 Nm^2 (the theoretical value has been calculated using CLPT equations) and thus there is a reduction of about 26% which cannot be neglected. The seams at the various points could not be modeled at the local level and thus a global adjustment had to take place in order for the model to have a rigidity value that corresponded to the actual specimen.

Table 3. Statistics of the FE model.

Material	Element type	No. of elements
Aluminum	SOLID45	5,520
Adhesive	SOLID45	5,520
Piezoelectric	SOLID5	5,520

Table 4. Modified material properties for reduced flexural rigidity used in Finite Element model.

	Piezoelectric	Substrate	Bond line	End supports
Elastic properties				
Material	PZT 5A	Alu 1100-H18	Hysol 9412	Glass Fiber
Density, ρ (kg/m^3)	7,800	2,700	2,400	1,600
Stiffness, E, (GPa)	41.5	47.6	0.68	50
Poisson's ratio, ν (−)	0.31	0.3	0.3	0.3
Piezoelectric properties				
d_{31} (m/V)	-320×10^{-12}			
d_{32} (m/V)	-320×10^{-12}			
d_{33} (m/V)	670×10^{-12}			

The procedure that was followed was simulating bending test using a pressure of $1\,\mathrm{N/mm}^2$. The modulus of elasticity of all materials has been reduced accordingly in order to have a flexural rigidity equal to $0.022\,\mathrm{Nm}^2$. Each of the materials were assumed to be isotropic (although it had to be introduced as anisotropic for the piezoelectric material due to ANSYS requirements with $E_{11} = E_{22} = E_{33}$ and $G_{12} = G_{23} = G_{13}$). The resulting properties used for the model are depicted in Table 4.

3.2. *Prestress static analysis*

In order to introduce prestress effects in the subsequent harmonic analysis and evaluate the effect of compressive forces into the dynamic response of the structure, a prestress static analysis has to take place. The prestress analysis for this model is taking place for four different compressive force values in order to be consistent with the experimental analysis. These forces are 0.8, 1.3, 1.8 and 2.3 N. Nonlinear effects (stress-stiffening) cannot be taken into account and this is due to the inherent incapability of ANSYS to perform a prestress calculation including nonlinear effects that can be later used for a prestressed harmonic analysis. This can be a major drawback that may reduce significantly the effect of the compressive forces over the subsequent harmonic analysis in case the analysis is entering the nonlinear area close to the critical buckling load. The critical buckling load for the present structure implementing the Euler formula is calculated at 4.1 N which permits the adoption of this assumption. The electrical boundary conditions for the piezoelectric layers are set to open circuit throughout the static analysis, thus only $V(x, y, t_{\mathrm{p}}) = V(x, y, t_{\mathrm{act}} - t_{\mathrm{p}}) = 0$. In closed circuit conditions (all piezoelectric faces are put to zero) the apparent rigidity of the structure is lower. However, the open circuit conditions seem to be more comparable to the actual experiment since these elements are never grounded during the experiment.

3.3. *Harmonic analysis*

A harmonic analysis was conducted by employing a sinusoidal forcing function of $+/-40\,\mathrm{V}$ from 0 through 30 Hz. Due to the extensive computational time that is

required it has been judged that performing a more detailed analysis with many time steps is more interesting instead of performing a less detailed analysis in a wider frequency domain. This frequency domain is divided into 150 equally spaced substeps, a parameter that is defined by the user. Obviously, the more substeps, the higher the resolution of the frequency domain and thus the peak amplitude at the resonance frequency is better depicted, especially for low damping values. The results that are obtained are depicted in Bode plots with the amplitude being normalized with respect to the displacement found at the lowest excitation frequency, which corresponds to the first of the 150 substeps that the frequency domain (0−30 Hz) is divided. This corresponds to a frequency of 0.2 Hz, thus a quasi-static excitation. The Bode plots amplitude is expressed by the following equation:

$$A = 20 \cdot \log_{10}(z/z_0). \tag{3.1}$$

All displacement values are measured at the point with coordinates $(L/2, b/2, t_{\text{act}})$. The damping value that is used is based on the experimental results and it is presented in Table 5. Additionally, a modal analysis was carried out in order to depict more accurately the frequency shift due to the axial loading. The harmonic analysis gives an estimation of the peak frequency (it depends on the resolution of the scanning of the frequency domain) while the modal analysis calculates exactly the natural frequencies of the structure. However, in the present analysis, due to the relatively large number of substeps, the harmonic analysis peak frequency and modal analysis results correlate very well.

4. Actuator Design and Experimental Setup

To examine the dynamic behavior of a typical PBP actuator a test setup was built. As test specimen a 230 mm long and 11.2 mm wide PBP actuator was constructed. The PBP actuator was made from an aluminum substrate with three PZT elements placed next to each other on each side of the substrate. To transfer bending stresses, style #120 glass fibercloth was applied on top of the seams between the elements as well as to the actuator end supports. Hysol 9412 was used as bonding and for the fiberglass matrix. To measure strain due to bending during the experiment, strain gauges were applied to the middle elements on either side of the actuator to measure the differential strain during excitation. The strain gauges were connected in a full Wheatstone bridge configuration. Figure 3 shows a schematic overview of the

Table 5. Damping and axial forces used in the numerical analyses.

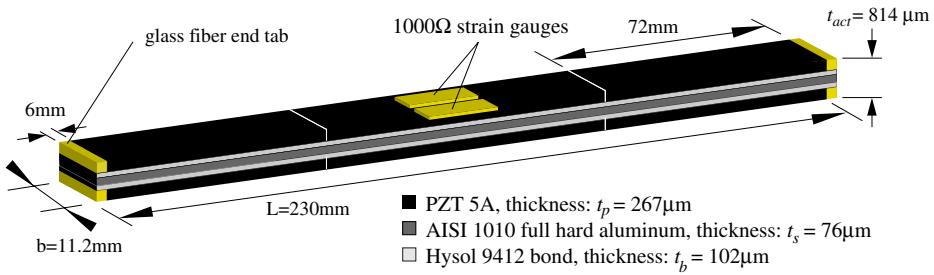| Analysis	Damping	Axial force (N)
1	0.05	0.8
2	0.07	1.3
3	0.10	1.8
4	0.13	2.3

Fig. 3. Schematic overview of the PBP actuator and dimensions.

actuator layup and dimensions and Table 2 shows the material properties of the actuator.

The test specimen was placed in an Instron 3345 test machine, where both sides of the actuator were pinned, as shown in Fig. 5. On the bottom side the test specimen was connected to a slide with a compression spring. In this way the axial force on the test specimen could be set by adjusting the clamp height of the tensile test machine. The force transducer on the Instron provided a 1 mN accurate force measurement of the axial force applied. The maximum axial force, F_a, applied to the specimen is given by:

$$F_a = kd. \tag{4.1}$$

5. Data Acquisition and Processing

The data acquisition and actuator control was done with a data acquisition device (DAQ). This device was controlled by the software package LabVIEW of National Instruments. To control the actuator, a sinusoidal control signal, $V(t)$, was used. The low-voltage control signal from the DAQ was amplified and supplied the actuator
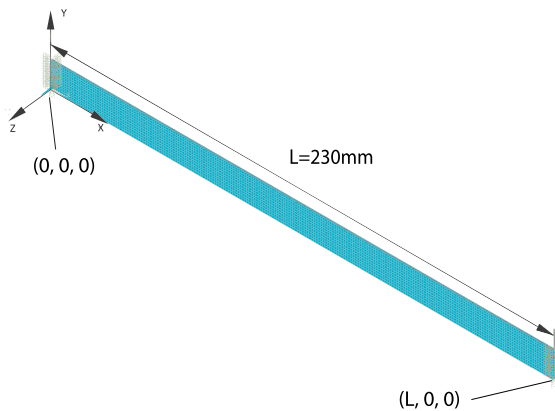

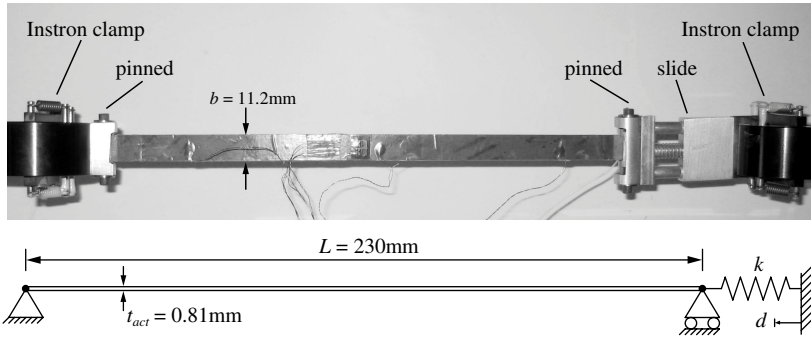Fig. 4. Finite element discretization of the PBP actuator.

Fig. 5. Front view photo and schematic side view of the setup.

with a signal of the form:

$$V(t) = V_{dc} + V_{amp}\sin(2\pi ft), \tag{5.1}$$

where the V_{dc} is a DC offset voltage, V_{amp} the amplitude of the signal and f the frequency in Hz. The actuator supply signal was given a DC offset voltage, V_{dc} such that the actuator showed symmetrical bending around the uncurved geometry. The necessary voltage to obtain this symmetry was 5V for any axial force and any V_{amp}. This was determined by measuring the axial force. Since the axial force is time dependent of the vertical displacement of the actuator tip, a straight position of the actuator led to the maximum axial force. The measurements were taken at various axial force levels. The axial force levels, F_a chosen for the experiment were 0.8, 1.3, 1.8, and 2.3 N. The maximum applied axial force was set to be 2.3 N, because when applying axial loads higher than 2.6 N the actuator began to exhibit snap-through behavior.

The resulting dynamic response of the actuator was measured by the DAQ by means of the differential voltage ΔV from the Wheatstone bridge. The DAQ also measured the current supplied to the actuator. The acquired data was processed in MATLAB with a least square method to determine the amplitude of the sinusoidal actuator response and the amplitude of the sinusoidal current signal. The strain at the midpoint of the actuator was calculated by relating the differential voltage ΔV to the differential resistance in a strain gauge, ΔR:

$$\frac{V_{wb} + \Delta V}{2V_{wb}} = \frac{R_{sg} + \Delta R}{2R_{sg}}, \tag{5.2}$$

where V_{wb} is the voltage over the Wheatstone bridge, 5 V and R_{sg} is the resistance of the strain gauge, which was 1,000 Ω. Knowing the gauge factor, GF, was 2.09, the strain was calculated according to[19]:

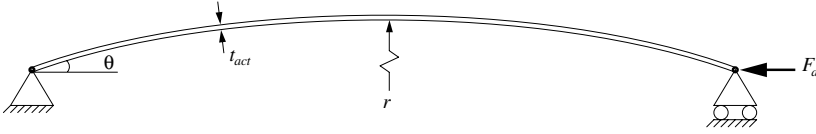$$\epsilon = \frac{\Delta R}{\text{GF}R_{sg}}. \tag{5.3}$$

Fig. 6. Schematic side view of a circular arc bent actuator.

To calculate the end rotation of the actuator, only first mode circular bending was assumed. Furthermore, it was assumed that the neutral line of the actuator coincided with the central line of the actuator, so that the strain on each side of the actuator was constant and opposite. From Fig. 6, the following relation can be derived assuming a circular arc shape function:

$$\theta\left(r + \frac{t_{\text{act}}}{2}\right) = \frac{L + \Delta L}{2}, \tag{5.4}$$

where r is the circular arc radius and θ the end rotation. Knowing that the strain is defined as the differential length ΔL divided by the total length L and that $r = L/2\theta$, the end rotation is calculated according to:

$$\theta = \frac{\Delta L}{t_{\text{act}}} = \frac{L}{t_{\text{act}}}\epsilon. \tag{5.5}$$

The end rotation in the measurements was corrected for an offset in strain. This offset was introduced in the strain gauges by the axial force and by imperfections in the actuator. Calibration at low frequency with laser reflection techniques, showed the end rotation calculated from the measured strain to correspond with the calibration within 10%.

6. Results and Discussion

In order to have a clear overview of the response of the structure under various axial loads, four different compressive forces have been evaluated (0.8, 1.3, 1.8, and 2.3 N) while a wide range of frequencies has been scanned. The electric input has an amplitude of $+/-40$ V. In any case the frequency range of interest is up to 30 Hz since critical phenomena such as resonance are taking place well below this frequency. Clearly the validation of the analytical and numerical models depends heavily on their performance concerning the produced displacement by the piezoelectric actuator. These results for the four compressive forces are shown in Figs. 7(a)−7(d). It is obvious that numerical and analytical methods results agree very well with experimental results in terms of the predicted natural frequency. Additionally, both numerical and analytical models grasp very well the normalized amplitude over the entire range of frequencies providing thus concrete evidence for their validity. Another conclusion from these plots is that although in absolute values, the displacement produced by the actuator is increasing with the increase of the axial load, for the normalized displacement this trend is inverted. The normalized
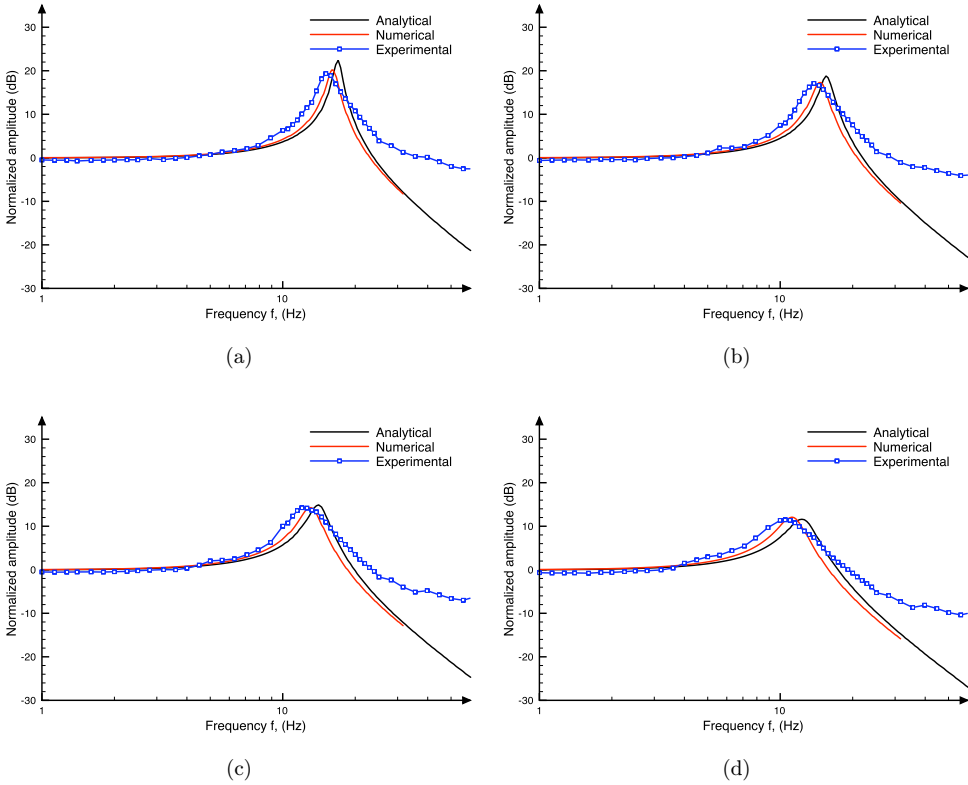
Fig. 7. Amplitude bode plot for (a) $F_a = 0.8\,\mathrm{N}$, (b) $F_a = 1.3\,\mathrm{N}$, (c) $F_a = 1.8\,\mathrm{N}$ and (d) $F_a = 2.3\,\mathrm{N}$.

displacement can be considered as an indication of the capacity of the actuator to amplify the quasi static response when operating in dynamic mode. This capability is decreased as the compressive force becomes higher due to the increase of the overall damping ratio of the structure. In order to clearly depict this trend, in Table 6 the natural frequencies, the damping values and the bode plot amplitude are presented for all three methods. It should be noted that in the regions of greatest interest to control systems engineers, the agreement is highest. Beyond $3 \times \omega_n$, the control system phase lag is typically so severe that control system design engineers generally do not count on commanding deflections in that region. Further, the experimental techniques used lead to reduced fidelity at higher frequencies.

In Table 6 the damping value for the numerical analysis is not calculated but it is in fact the input value that has been used. Clearly, the calculation of the overall damping of the structure cannot be achieved by the numerical models. There are various parameters (hinge friction, material hysteresis, piezoelectric domain switching, Coulomb damping etc.) that cannot be accurately evaluated and thus introduced in the numerical model. Local models with high detail could grasp these mechanics and then with the application of hierarchical modeling principles these

Table 6. Damping, Natural Frequencies and Bode amplitude for Numerical, Analytical and Experimental analyses (* means that it has been extracted from experimental results).

Axial force	Quantity	Analytical	Numerical	Experimental
0.8	A_n	22.00	20.20	19.35
	ω_n	16.95	16.13	15.20
	ζ	$\alpha = 28$	0.05^*	0.05
1.3 N	A_n	18.80	17.29	17.09
	ω_n	15.62	14.50	13.80
	ζ	$\alpha = 28$	0.07^*	0.07
1.8 N	A_n	14.30	14.28	14.25
	ω_n	14.16	13.10	12.50
	ζ	$\alpha = 28$	0.10^*	0.10
2.3 N	A_n	11.50	12.08	11.47
	ω_n	12.53	11.20	10.60
	ζ	$\alpha = 28$	0.13^*	0.13

could have been introduced in the global model. However, this endeavor exceeds the scope of the present work.

Similar conclusions can be extracted from the end rotation bode plots shown in Fig. 8. The trend that is depicted here is the same as in the case of amplitude. However, for the lowest value of the axial force the discrepancy between the modeling methods (analytical − numerical) and the experimental analysis seems to be quite substantial. For higher axial forces this discrepancy is lower and for the case of 2.3 N it seems that there is excellent agreement between these two methods. It is important to mention at this point that for the numerical analysis the end rotation is measured through the relative displacement of the first aluminum/bond line interface with respect to the boundary condition ($u_x = 0$). However, using this method the shear between the layers (although limited due to the small thickness of the structure) is included in this measurement and thus the result is not pure rotation. Additionally
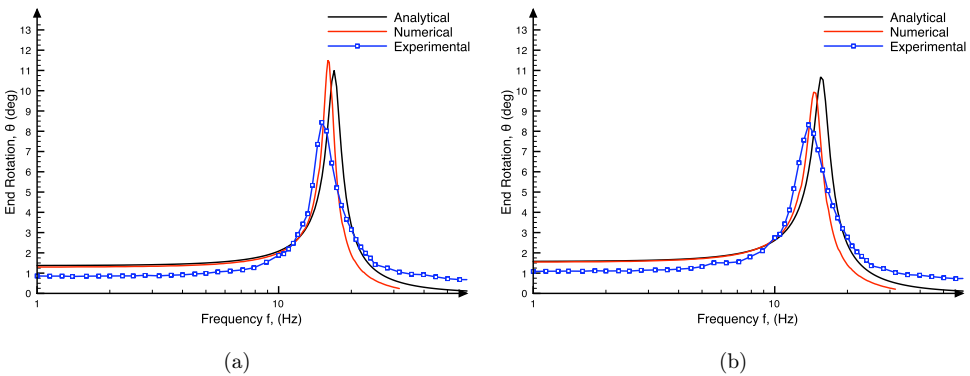

(a)　　　　　　　　　　　　　　　　(b)

Fig. 8. End rotation plot for (a) $F_a = 0.8\,\mathrm{N}$, (b) $F_a = 1.3\,\mathrm{N}$, (c) $F_a = 1.8\,\mathrm{N}$ and (d) $F_a = 2.3\,\mathrm{N}$.
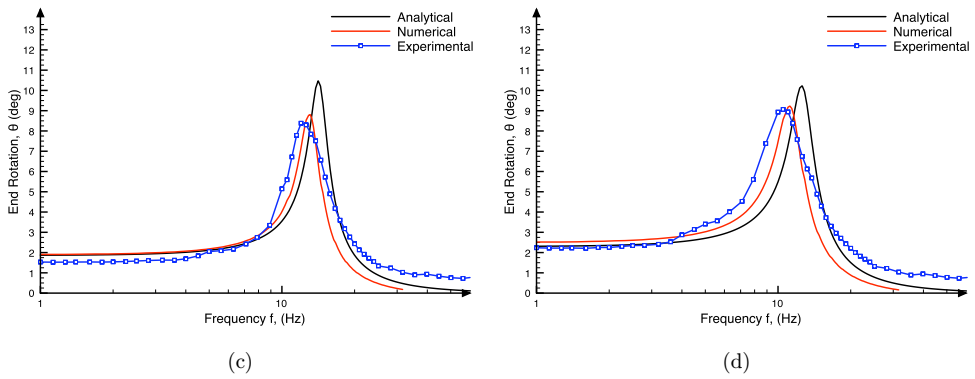
(c)

(d)

Fig. 8. (*Continued*)

one should not forget that in the numerical and analytical analysis the structure is assumed to be continuous with reduced flexural rigidity in order to simulate the effect of the seams. However, in the experimental procedure this is not the case and the structure has a discontinuity at the area of the seams. The reduced capacity of
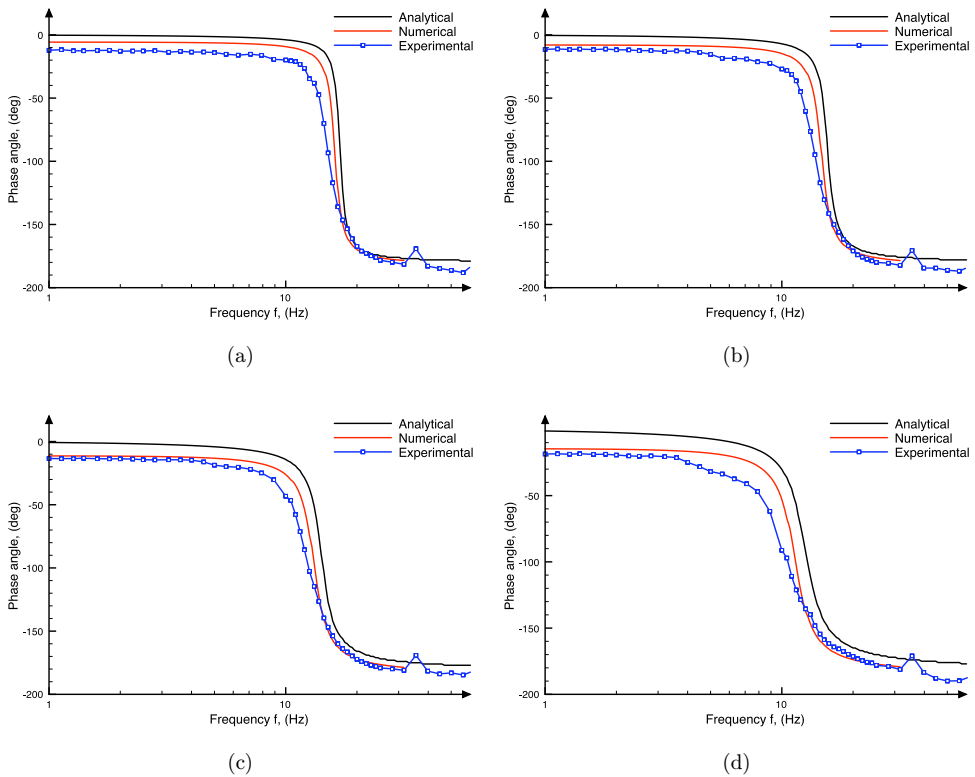

(a)

(b)

(c)

(d)

Fig. 9. Phase lag plot for (a) $F_a = 0.8\,\text{N}$, (b) $F_a = 1.3\,\text{N}$, (c) $F_a = 1.8\,\text{N}$ and (d) $F_a = 2.3\,\text{N}$.

the structure at this point to carry the bending moment results in reduced flexural bending at the supports and thus reduced end rotation.

Apart from the amplitude and end rotation bode plots, the corresponding plots for the phase shifting are depicted for the various axial loads in Figs. 9(a)−9(d). The system exhibits a second order behavior with phase shifting of $180°$ beyond the natural frequency. In these graphs one can see that the phase shifting exists already even at very low frequencies. At 1 Hz, there is already a difference in the phase angle between the four graphs that correspond to the different compressive forces. For the experimental analysis this can be attributed to the piezoelectric material hysteresis, while in the case of the numerical analysis it can be attributed to the static prestress solution that precedes the harmonic analysis. In the analytical results, these phenomena are not included and the phase shift is purely related to the characteristics of the system.

7. Conclusions

The aim of the present work has been to introduce the analytical and numerical models that are capable of predicting the dynamic performance of PBP actuators over a wide range of the frequency domain. It has been clearly demonstrated that the normalized amplitude of the PBP actuator drops with the increase of the axial force. This is the case for the natural frequency of the actuator, while the damping ratio is substantially increased. Obviously the phase lag is alternated as well. Analytical and numerical models seem to grasp very well the dynamics of the PBP actuators over the studied frequency range. The natural frequency shift has been evaluated with accuracy by both types of models, while their validity has been confirmed by the experimental results on a 230 mm PBP actuator. The damping ratio extracted from the experimental procedure has been introduced in the numerical model and it has been possible to predict with high accuracy the normalized amplitude of the actuator. It seems also that the damping ratio follows a quasi-linear behavior with respect to the axial load. More tests with different axial forces (in any case away from the critical buckling load to avoid geometrical nonlinearity) could provide valuable data for the damping behavior with respect to the applied axial force. In any case, it seems that the use of PBP actuators for actuation applications that require dynamic performance is within their operational envelope. However, it is also clear that the drop of the natural frequency dictates that the designer has to trade bandwidth for deflection.

References

1. R. Barrett, R. S. Gross and F. Brozoski, Missile flight control using active flexspar actuators, *SPIE* **2443** (1995) 52−61.
2. R. Barrett, Active aeroelastic tailoring of an adaptive flexpar stabilator, *J. Smart Materials and Structures* **5**(6) (1996) 723−730.
3. R. Barrett and J. Stutts, Design and testing of a 1/12th scale solid state adaptive rotor, *J. Smart Materials and Structures* **6**(4) (1997) 491−497.
4. R. Barrett, P. Frye and M. Schliesman, Design, construction and characterization of a flightworthy piezoelectric solid state adaptive rotor, *J. Smart Materials and Structures* **7**(3) (1998) 422−431.
5. R. Barrett and R. Vos, Post-buckled precompressed (PBP) subsonic micro flight control actuators and surfaces, *J. Smart Materials and Structures* **17**(5) (2008).
6. G. Lesieutre and C. Davis, Can a coupling coefficient of a piezoelectric actuator be higher than those of its active material?, *J. Intell. Mat. Syst. Str.* **8**(10) (1997) 859−867.
7. G. Giannopoulos, J. Monreal and J. Vantomme, Snap-through buckling behavior of piezoelectric bimorph beams: I. Analytical and numerical modeling, *J. Smart Materials and Structures* **16**(4) (2007) 1148−1157.
8. G. Giannopoulos, J. Monreal and J. Vantomme, Snap-through buckling behavior of piezoelectric bimorph beams: II. Experimental verification, *J. Smart Materials and Structures* **16**(4) (2007) 1158−1163.
9. C. Maurini, J. Pouget and S. Vidoli, Distributed piezoelectric actuation of a bistable buckled beam, *Eur. J. Mech. A-Solid.* **26**(5) (2007) 837−853.
10. R. Vos, R. De Breuker, R. Barrett and P. Tiso, Morphing wing flight control via post-buckled precompressed piezoelectric actuators, *J. Aircraft* **44**(4) (2007) 1060−1068.
11. R. Vos, R. Barrett, M. Van Tooren and L. Krakers, Post-buckled precompressed (PBP) piezoelectric actuators for UAV flight control, *SPIE* **6173** (2006) 61730E.1−61730E.12.
12. R. De Breuker, P. Tiso, R. Vos and R. Barrett, Nonlinear semi-analytical modeling of post-buckled precompressed (PBP) piezoelectric actuators for UAV flight control, in *Proc. 47th AIAA/ASME/ASCE/AHS/ASC Structures, Structural Dynamics, and Materials Conf.* (Newport, RI, USA, 2006).
13. R. Barrett, R. McMurtry, R. Vos, P. Tiso and R. DeBreuker, Post-buckled precompressed (PBP) elements: A new class of flight control actuators enhancing high speed autonomous VTOL MAVs, *SPIE* **5762** (2005) 111−122.
14. R. Barrett, R. McMurtry, R. Vos, P. Tiso and R. DeBreuker, Post-buckled precompressed piezoelectric flight control actuator design, development and demonstration, *J. Smart Materials and Structures* **15**(5) (2006) 1323−1331.
15. M. Groen, M. van Schravendijk, R. Barrett and R. Vos, Advanced control techniques for post-buckled precompressed (PBP) flight control actuators, in *Proc. SPIE Smart Materials Structures Symposium* (San Diego CA, USA, 2009).
16. W. T. Thomson and M. D. Dahleh, *Theory of Vibrations with Applications*, 2nd edn. (Prentice Hall, New Jersey, 1998).
17. A. L. Kimball, Vibration damping including the case of solid damping, *Transactions ASME, APM* (1929), pp. 51−52.
18. R. Jones, *Mechanics of Composite Materials* (Scripta Book Company, Washington, D.C., 1975).
19. T. G. Beckwith, R. D. Marangoni and V. Leinhard, *Mechanical Measurements*, 5th edn. (Addison-Wesley Publishing, Reading, MC, 1993).